nature communications

Article

https://doi.org/10.1038/s41467-024-53625-3

Covalent organic framework membranes with vertically aligned nanorods for efficient separation of rare metal ions

Received: 24 June 2024

Accepted: 14 October 2024

Published online: 25 October 2024

Check for updates

Qinghua Liu[1], Ming Liu[1], Zhe Zhang[2] ✉, Congcong Yin[3], Jianghai Long[1], Mingjie Wei[1] & Yong Wang[1,3] ✉

Covalent organic frameworks (COFs) have emerged as promising platforms for membrane separations, while remaining challenging for separating ions in a fast and selective way. Here, we propose a concept of COF membranes with vertically aligned nanorods for efficient separation of rare metal ions. A quaternary ammonium-functionalized monomer is rationally designed to synthesize COF layers on porous substrates via interfacial synthesis. The COF layers possess an asymmetric structure, in which the upper part displays vertically aligned nanorods, while the lower part exhibits an ultrathin dense layer. The vertically aligned nanorods enlarge contact areas to harvest water and monovalent ions, and the ultrathin dense layer enables both high permeability and selectivity. The resulting membranes exhibit exceptional separation performances, for instance, a Cs^+ permeation rate of 0.33 mol m^{-2} h^{-1}, close to the value in porous substrates, and selectivities with Cs^+/La^{3+} up to 75.9 and 69.8 in single and binary systems, highlighting the great potentials in the separation of rare metal ions.

Covalent organic frameworks (COFs) permit multifunctional platforms for designing functional materials with well-defined architectures toward task-specific applications, including energy storage, catalysis, separation, and purification[1–4]. COFs are synthesized through topology-guided reticulation processes, in which knots and linkers are covalently linked with particular linkages to form extended frameworks[5–7]. These features allow COFs to have permanent porosity and to be architecturally robust, giving rise to numerous merits, including uniform porosities, high surface area, tailorable pore size, and chemistries, as well as excellent hydrolytic stability[8–10]. Especially, the innate nanopores and adjustable wall chemistries make COFs promising candidates as advanced membranes for ion separations.

To construct COF membranes, an overarching challenge to overcome is how to prepare them under mild conditions without sacrificing porosity and crystallinity—the most essential characteristics[11]. Interfacial synthesis is widely explored as a convenient and delicate protocol, with which COFs are crystallized at a confined and stable oil–water interface to afford continuous membranes under ambient conditions[12]. Unlike conventional ion separation membranes, for example, polyamide membranes, synthesized by irreversible and instantaneous interfacial polymerization[13], COFs are formed by reversible reactions that require much longer periods of time for creating continuous membranes[11]. The extended synthesis duration allows COFs to accomplish the self-repairing process to substantially improve the crystallinity and porosity[14], but meanwhile, the thickness of COF membranes would be increased to a large extent. So far, thick COF membranes with thicknesses ranging from hundreds of nanometers to several microns have been proven to have high crystallinity, large surface area, and mechanically robust[15–19]. However, the large thickness inevitably increases mass transport resistance that results in impeded permeation[20], which is not favorable for ion separations.

[1]State Key Laboratory of Materials-Oriented Chemical Engineering, and College of Chemical Engineering, Nanjing Tech University, Nanjing 211816 Jiangsu, China. [2]School of Environmental Science and Engineering, Nanjing Tech University, Nanjing 211816 Jiangsu, China. [3]School of Energy and Environment, Southeast University, Nanjing 210096 Jiangsu, China. ✉e-mail: zhangzhe@njtech.edu.cn; yongwang@seu.edu.cn

It is widely considered that ultrathin membranes can maximize the permeation in a straightforward way[21–23]. Additive-mediated crystallization[21,24], nanosheet stacking[25,26], and electrophoretic deposition[27,28] have been shown to create ultrathin COF membranes, the thickness of which is usually less than 100 nm. Although the permeation can be significantly enhanced, ultrathin membranes are highly susceptible to structural failure being exposed to larger stress[29,30]. Other concerns regarding ultrathin COF membranes involve the difficulty of avoiding defects and the ambiguity in crystallinity and porosity control[16,31,32]. Based on the above considerations, a better COF membrane must have the following characteristics: (1) it should exhibit high permeability and tight selectivity; and (2) it should be highly crystalline, porous, and mechanically robust.

Herein, we explore COF membranes featuring vertically aligned nanorods for efficient separation of rare metal ions (Fig.1). A quaternary ammonium-functionalized monomer with positive charges was designed and synthesized to afford COF layers with vertically aligned nanorods on porous substrates through interfacial synthesis. The COF layers are asymmetrically structured, exhibiting vertically aligned nanorods on the upper part and an ultrathin-dense layer on the lower part. The vertically aligned nanorods of the upper part not only enlarge contact areas to harvest water and smaller ions but also eliminate defects. The ultrathin dense layer of the lower part enables both high permeability and selectivity. Moreover, the substrate provides mechanical robustness to protect the lower part, as the ultrathin dense layer was sandwiched between the substrate and the vertically aligned nanorods. Importantly, this unique structure is distinct from the previous work reporting randomly stacked COF nanorods[33], as the COF layer in the present work is composed of vertically aligned nanorods that are connected with each other by a continuous film. The resultant COF membranes show fast permeation of water molecules and monovalent ions, along with an exceptional selectivity for rare metal ions. This work not solely explores an engineering concept for the construction of high-performance COF membranes but highlights the great potential of COF membranes in the separation of rare metal ions.

Results

Fabrication and characterization of COF membranes

A quaternary ammonium-functionalized aldehyde monomer with a positive charge was rationally designed and synthesized by grafting an ionic liquid compound, 2-bromoethyltrimethylammonium bromide (AB), onto a C_3-symmetric 2-hydroxy-1,3,5-benzenetricarbaldehyde (HB) building block via the Williamson ether synthesis. This monomer was termed HBAB, and the chemical structure was verified by ^{1}H nuclear magnetic resonance spectroscopy and high-resolution mass spectrometry (Supplementary Fig. 1). COFs can be synthesized via a Schiff-base reaction between the HBAB monomer and a C_3-symmetric 2,4,6-tri(4-aminophenyl)−1,3,5-triazine (TAPA) building block, and the product was named as HBAB-TAPA-COF (Fig. 2). Considering the unique molecular structure of the HBAB monomer and the need for charges being uniformly distributed, each pore in the HBAB-TAPA-COF monolayer carried only one quaternary ammonium group. Thus, the quaternary ammonium groups in the one-dimensional channel of the HBAB-TAPA-COF would display a staggered alignment between adjacent monolayers.

We synthesized HBAB-TAPA-COF layers on hydrolyzed polyacrylonitrile (HPAN) substrates via interfacial synthesis. Beforehand, the solubility of monomers in water and *n*-butanol serving as the aqueous and organic phase solvents was investigated. The HBAB monomer was both soluble in water and in *n*-butanol, while the TAPA monomer was soluble in *n*-butanol, insoluble in water (Supplementary Fig. 2). Thus, the HBAB monomer dissolving in water was used as the aqueous phase, while the TAPA monomer dissolving in *n*-butanol was used as the organic phase. The two-phase solutions were filled in a synthesis device, in which the HPAN substrate was mounted in the middle with the upper surface toward the organic phase (Fig. 3a). After 72 h of the reaction, the color of the front of the substrate turned to dark red, indicating a unidirectional diffusion of the HBAB monomer from the aqueous phase to the organic phase (Fig. 3a and Supplementary Fig. 3). From the scanning electron microscopy (SEM) and the atomic force microscopy (AFM) images (Fig. 3b, c and Supplementary Fig. 4), the nanorods grown on the substrate were found to be vertically aligned. Grazing incidence wide-angle X-ray scattering (GIWAXS) measurement was further conducted to demonstrate the orientation of the nanorods[34]. Figure 3d displays bright scattering rings, in which the out-of-plane reflections were significantly stronger than the in-plane reflections, indicating the HBAB-TAPA-COF nanorods were perpendicular to the substrate surface over a large area[35]. We used *N,N*-dimethylformamide as the etching solvent to remove the HPAN substrate, and a free-standing HBAB-TAPA-COF layer can be released and floated on the liquid surface. The released layer was then attached to an anodic aluminum oxide substrate to conduct an examination with energy-dispersive X-ray (EDX) spectroscopy. The EDX element mapping demonstrated uniformly distributed carbon element traversing the entire cross-section of the HBAB-TAPA-COF layer (Supplementary Fig. 5). Furthermore, the cross-sectional SEM image and the transmission electron microscopy (TEM) image (Fig. 3e, f) also verified the vertically aligned nanorods of the HBAB-TAPA-COF exclusively formed on the HPAN substrate, and the thickness was measured to be ~1 µm.

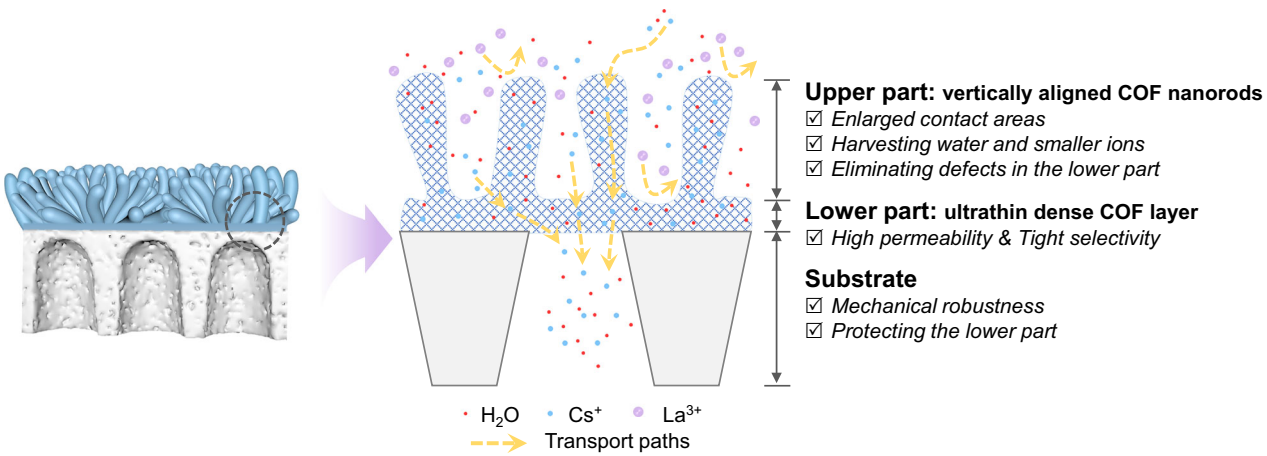

Fig. 1 | Schematic diagram of the asymmetric structure of the COF membrane ensuring fast and selective ion separations. COF layers are formed on a porous substrate via interfacial synthesis. The COF layer is composed of the upper part with vertically aligned COF nanorods and the lower part with an ultrathin-dense COF layer.

https://doi.org/10.1038/s41467-024-53625-3

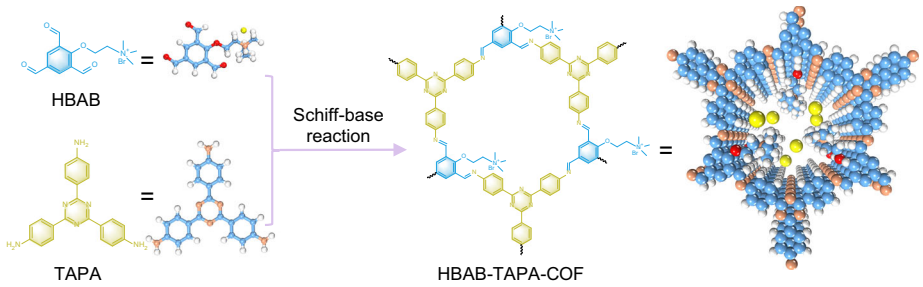

Fig. 2 | Schematic diagram of the synthetic route of the HBAB-TAPA-COF. The HBAB-TAPA-COF is synthesized through a Schiff-base reaction between the aldehyde monomer (HBAB) and the amine monomer (TAPA).

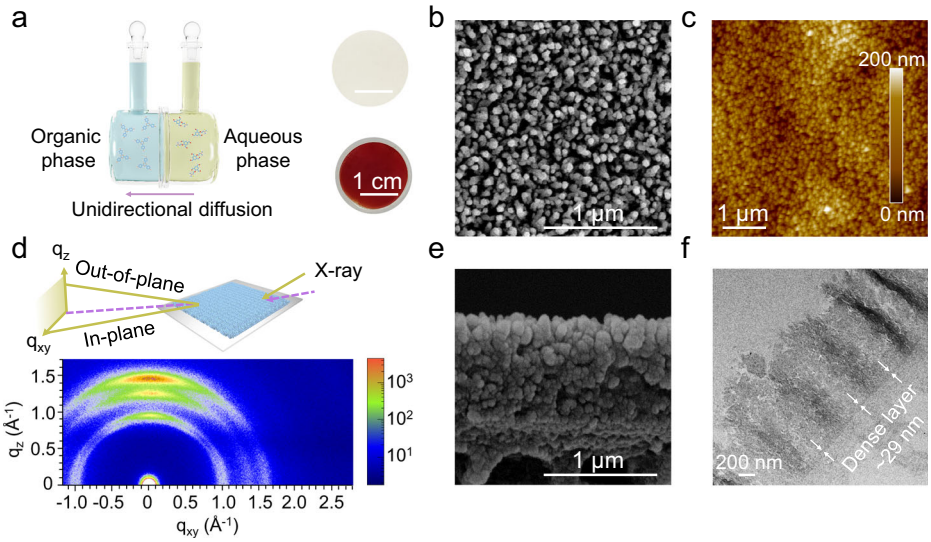

Fig. 3 | Microstructures of HBAB-TAPA-COF layers. a Schematic diagram of the interfacial synthesis. The insert shows digital images of the pristine (upper right) and the HBAB-TAPA-COF layer grown on the HPAN substrate (bottom right). **b** Surface SEM and **c** AFM images. **d** GIWAXS patterns. The insert shows the schematic diagram of GIWAXS measurement. **e** Cross-sectional SEM image. **f** Cross-sectional TEM image.

Notably, after removing the substrate, the rear surface morphology of the HBAB-TAPA-COF layer was somewhat similar to that of the top surface, but the nanorods were densely packed without any gaps or voids (Supplementary Fig. 6). Therefore, The HBAB-TAPA-COF layer possessed an asymmetric structure, in which the upper part displayed the vertically aligned nanorods, while the lower part exhibited an ultrathin dense layer with a thickness of ~29 nm (Fig. 3f and Supplementary Fig. 7). The HBAB-TAPA-COF layer tightly adhered on the substrate which showed good mechanical stability, as no cracking or peeling occurred after being bent and folded (Supplementary Fig. 8).

The chemical structure of the HBAB-TAPA-COF layer was confirmed by the Fourier transform infrared (FTIR) spectroscopy (Fig. 4a). The vibrational bands at 1677 cm^{-1} (C=O) and 3323 cm^{-1} (N-H) belonging to the monomers were absent in the spectrum of the HBAB-TAPA-COF, while the vibrational bands at 1627 cm^{-1} assigned to C=N of the imine linkage emerged, indicating the complete conversion from the monomers to the final product. The chemical structure of the HBAB-TAPA-COF layer was further verified by X-ray photoelectron spectroscopy (XPS) (Fig. 4b). The result indicated that the nitrogen elements of C=N, C–N, and N^+ followed a ratio of 2:1:1, which is consistent with the theoretical structure of the HBAB-TAPA-COF[36]. For comparison of the crystallinity and porosity, we also synthesized HBAB-TAPA-COF powders under solvothermal conditions. From X-ray diffraction (XRD) pattern (Fig. 4c), HBAB-TAPA-COF membranes displayed XRD peaks at 5.5°, 9.8°, 11.3°, and 26.4°, which can be assigned to (100), (110), (200) and (001) planes, respectively. This result was in accordance with that of the powders (Supplementary Fig. 9). Note that the characteristic diffraction peaks of the ionic liquid compound did not appear in the XRD pattern of the HBAB-TAPA-COF (Supplementary Fig. 10). We further used Materials Studio to find out the possible structure of the HBAB-TAPA-COF (Supplementary Table. 1). Pawley refinement regenerated the XRD pattern with small residue (Rwp = 5.44%, Rp = 3.43%), and thus the HBAB-TAPA-COF exhibited an eclipsed AA model that contained a space group of P_6/mmc ($a = b =$ 18.7121 Å, c = 3.4416 Å, $\alpha = \beta = 90°$, and $\gamma = 120°$). This is well in line with the experimental pattern, indicating the highly crystalline nature of the HBAB-TAPA-COF. Nitrogen adsorption-desorption measurement was used to investigate the porosity of the HBAB-TAPA-COF layer (Fig. 4d). Since the HBAB-TAPA-COF layer on the substrate was very difficult to be isolated for testing, its free-standing counterpart was prepared from a free oil-water interface using the same protocol. The n-butanol and water served as the organic and aqueous phases, respectively, so that a continuous membrane could be crystallized at the confined interface (Supplementary Fig. 11a). The surface of such membrane exhibited similar morphology, in which nanorods were formed but were not vertically aligned (Supplementary Fig. 11b). As shown in Fig. 4d, e, at the low relative pressure, the HBAB-TAPA-COF exhibited rapid uptake of nitrogen, which was consistent with the type I isotherm, indicating abundant microporous structures of the HBAB-TAPA-COF. The results also showed that the Brunauer-Emmett-Teller (BET) surface area of the HBAB-TAPA-COF membrane was as high as 812 $m^2 g^{-1}$, and the pore size was centered at 1.2 nm calculated from nonlocal density functional theory (NLDFT) model[37]. Moreover, HBAB-TAPA-COF powders exhibited a slightly higher surface area of

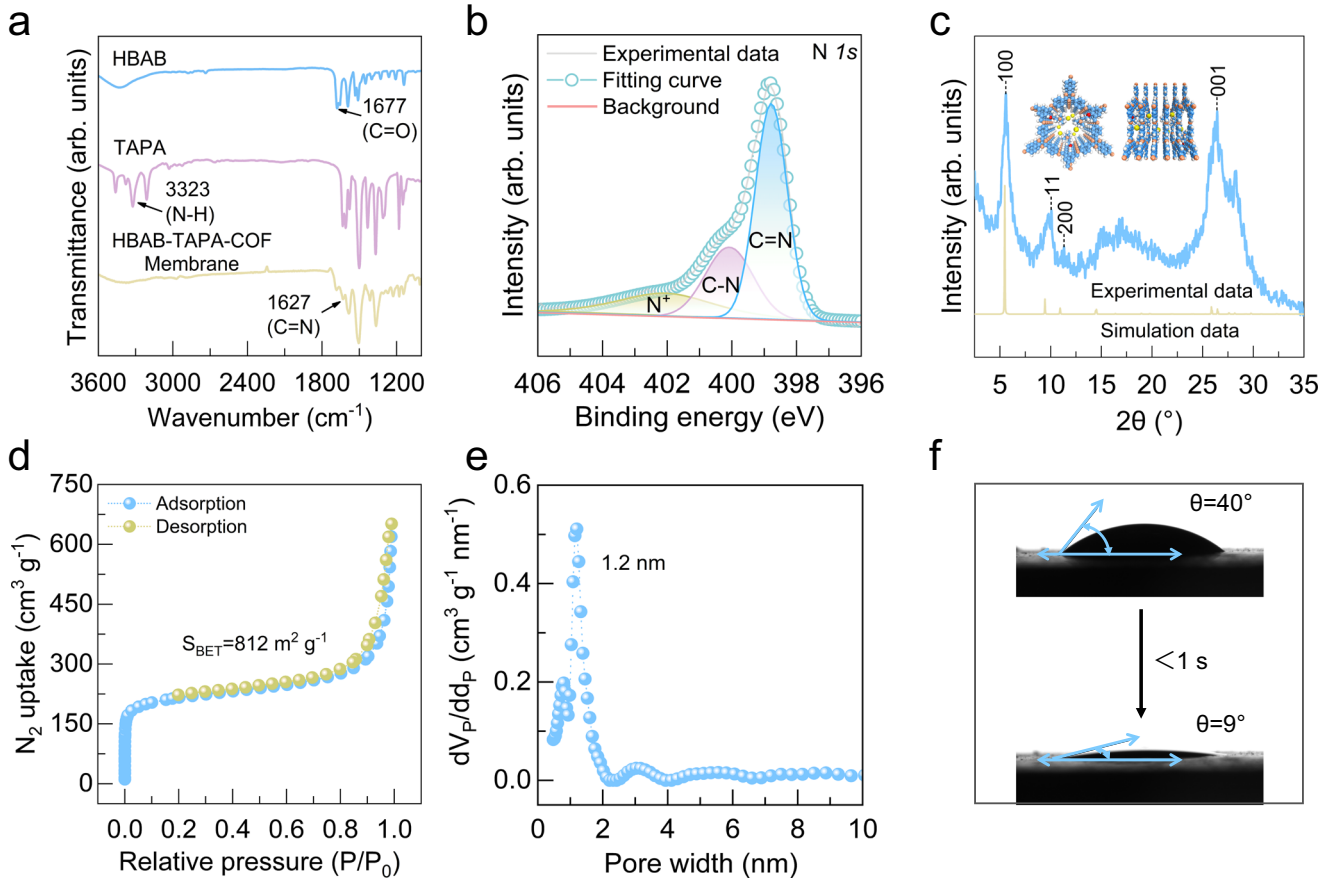

Fig. 4 | Physicochemical properties of HBAB-TAPA-COF layers. a FTIR spectra. **b** XPS spectra. **c** XRD patterns. The insert shows the structural modes of the HBAB-TAPA-COF. **d** Nitrogen adsorption-desorption isotherms and **e** corresponding pore size distribution curve. **f** Water contact angle images.

869 $m^2 g^{-1}$ with a same pore size of 1.2 nm, demonstrating the highly porous properties of the HBAB-TAPA-COF (Supplementary Fig. 12). Due to the vertically aligned nanorods with enlarged contact areas, abundant microporous structures and hydrophilic quaternary ammonium groups, the HBAB-TAPA-COF layer exhibited excellent wettability, as water molecules can penetrate through the layer within merely 1 s (Fig. 4f). In addition, because the quaternary ammonium group was positively charged, the HBAB-TAPA-COF layer showed stronger positive charge than that of the HPAN substrate (Supplementary Fig. 13). The thermogravimetry analysis revealed that the HBAB-TAPA-COF was stable up to 400 °C under nitrogen atmosphere, while a slight weight loss at ~100 °C can be ascribed to the water loss stemming from the highly hydrophilic nature (Supplementary Fig. 14). It should note that although the ionic liquid compound was very difficult to be thoroughly removed, no significant residue of ionic liquid compound existed, and the crystallinity and the porosity were not compromised.

Dissecting the formation mechanism of vertically aligned nanorods

To illustrate the underlying mechanism of the formation of the vertically aligned nanorods of the HBAB-TAPA-COF, we investigated the morphological variations under different synthesis duration using SEM and TEM imaging (Fig. 5 and Supplementary Fig. 15). At the synthesis duration of 6 h, small and discretely distributed nanorods with a thickness of 192 nm appeared on the HPAN substrate, but they did not form a continuous layer as the substrate pores still can be seen. When the synthesis duration was prolonged to 12, 24, 48, and 72 h, respectively, their surfaces all exhibited a very similar morphology with vertically aligned nanorods. Moreover, the thicknesses increased from 219 nm to 292, 500, and 992 nm, respectively, with prolonging the synthesis duration. From SEM images of the rear surfaces, gaps, and voids can be clearly seen at the synthesis duration of 6, 12, 24, and 48 h. However, with the duration prolonging, those defects began to disappear, and a continuous and defect-free layer was obtained at the duration of 72 h, as mentioned previously. Therefore, the thickness of the HBAB-TAPA-COF layer continued to increase with prolonging the synthesis duration, while the diameter of the nanorods did not change markedly (Supplementary Fig. 16). This phenomenon can be explained by the reversible reactions of COFs typically required longer durations to create defect-free membranes, and the self-limiting effect would occur at the end of the synthesis. In addition to the synthesis duration, the effects of various concentrations of HBAB monomers on the morphology were also investigated (Supplementary Fig. 17). The HBAB-TAPA-COF prepared under different concentrations have a similar morphology compared with that under a synthesis duration of 72 h. With increasing the concentrations from 0.29 to 0.44, 1.74, and 2.61 mM, the HBAB-TAPA-COF gradually became thicker, while the increase in thicknesses was not very pronounced compared to the scenario of synthesis duration. We also tried to prepare HBAB-TAPA-COF layers using different substrates, including PAN, AAO, and polyimide (Supplementary Fig. 18), however, none of them showed consistent morphology with HAPN, suggesting that the HPAN substrate played an important role in the formation of vertically aligned nanorods of the HBAB-TAPA-COF. Furthermore, other amine monomers with an analogous molecular structure to the TAPA monomer, including 1,3,5-tris(4-aminophenyl) benzene, tris(4-aminophenyl) amine, and tris(4-aminophenyl) methane were also used to synthesize COF membranes using the same protocol. Similarly, those amine monomers were soluble in *n*-butanol but insoluble or partially soluble

https://doi.org/10.1038/s41467-024-53625-3

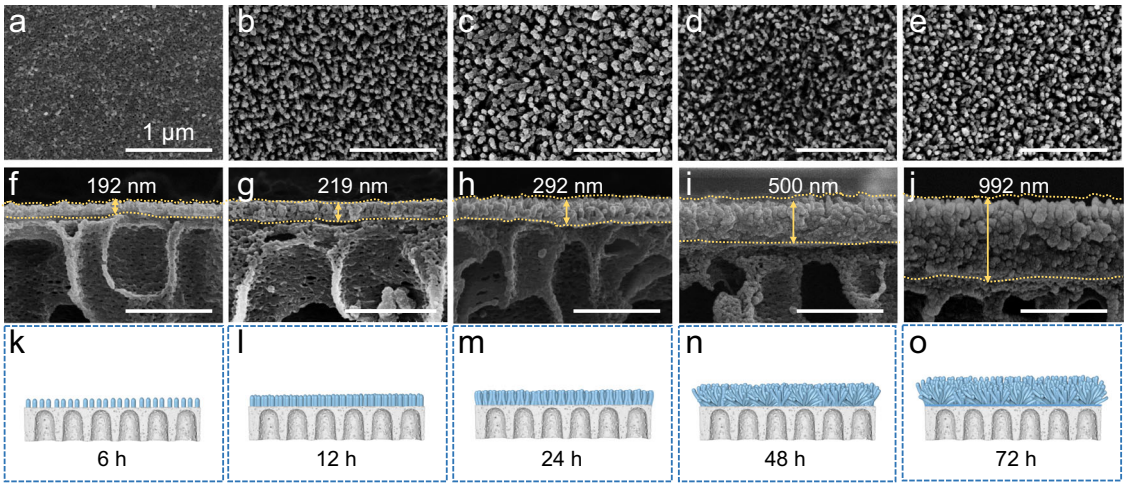

Fig. 5 | SEM images of surface, cross-section, and corresponding schematic diagrams. HBAB-TAPA-COF layers synthesized from the synthesis duration at 6 h (**a**, **f**, **k**), 12 h (**b**, **g**, **l**), 24 h (**c**, **h**, **m**), 48 h (**d**, **i**, **n**), 72 h (**e**, **j**, **o**). **a**–**e** Surfaces. **f**–**j** Cross-sections. **k**–**o** Corresponding schematic diagrams. The scale bar in **a**–**j** is 1 μm.

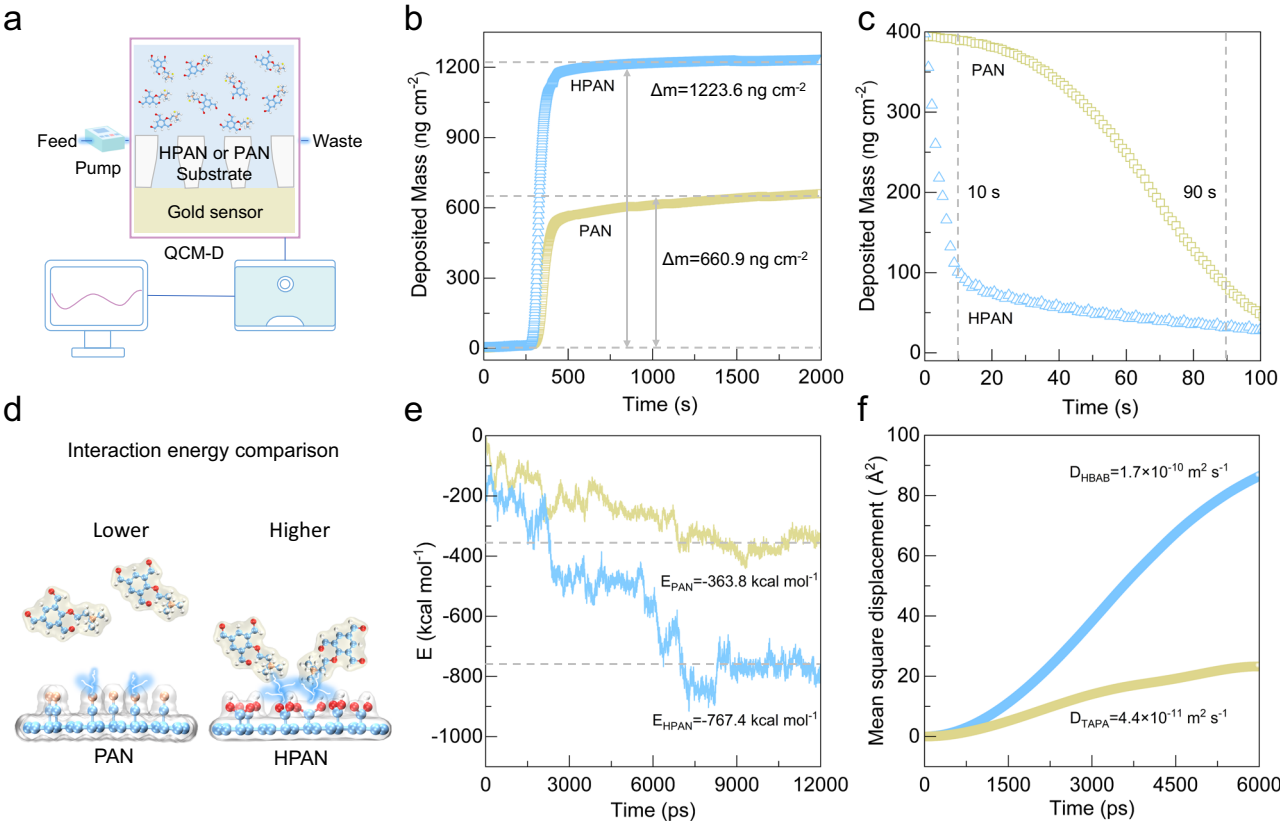

Fig. 6 | QCM-D analysis and MD simulations. a Schematic diagram of QCM-D. **b** QCM-D absorption test of HBAB monomers on the HPAN and the PAN. **c** Desorption test of HBAB monomers from the HPAN and the PAN. **d** Schematic diagram depicting the interaction energy between the HBAB monomer and different substrates. **e** Variation of interaction energies with time. **f** Variation of the MSD with time.

in water (Supplementary Fig. 19). After interfacial synthesis, COFs were successfully grown on HPAN substrates, which exhibited vertically aligned nanorods, even though the nanorods were slightly short (Supplementary Fig. 20). Above findings indicated that the HBAB monomer and the HPAN substrate may play a vital role on the formation of the vertically aligned nanorods.

We further examined the interplays between HBAB monomers and the HPAN substrate. Since HBAB-TAPA-COF layers were exclusively formed on the upper surface of the HPAN substrate after the reaction, HBAB monomers are expected to experience a unidirectional transport diffusing from the aqueous phase to the organic phase. Quartz crystal microbalance with dissipation (QCM-D) technique was conducted to analyze the adsorption and desorption of the HBAB monomer by HPAN and PAN layers coated on quartz crystal sensors[38,39] (Fig. 6a). The HPAN showed a significantly enhanced adsorption of the HBAB monomer (Fig. 6b), which was roughly doubled compared to that of the PAN (660.9 ng cm^{-2} for the PAN, and 1223.6 ng cm^{-2} for the HPAN), demonstrating the key role in the uptake of the HBAB

monomer. This can be mainly attributed to the electrostatic interaction between the positively charged HBAB monomer and the HPAN having abundant carboxyl groups. For desorption, the HPAN showed rapid release of the HBAB monomer within 10 s (Fig. 6c), while the PAN exhibited a much lower rate. It seems counterintuitive that a substrate having the ability to adsorb more monomers could release it rapidly. This can be explained by the unique molecular structure of HBAB bearing only one quaternary ammonium group, as mentioned previously. Although the HPAN substrate with negative charges was capable of binding the HBAB monomer via electrostatic interaction, only one quaternary ammonium group did not possess enough positive charge and thus could not be firmly bonded with the HPAN substrate. As a result, the HBAB monomer can be adsorbed by the HPAN substrate first, while would be released rapidly, leading to continuous diffusion from the aqueous solution to the organic solution.

A molecular dynamic (MD) simulation was performed to reveal the relationship between HBAB monomers and the HPAN substrate. We calculated the interaction energies of HBAB monomers with two kinds of substrates (Fig. 6d, e). Higher interaction energy was evidently observed for the HPAN substrate rather than the PAN substrate (−363.8 kcal mol^{-1} for the PAN, and −767.4 kcal mol^{-1} for the HPAN). Such higher interaction between HBAB and HPAN indicated that HBAB monomers adsorbed to HPAN substrate in larger amounts, which agreed with the result from the QCM-D measurement. Once the HBAB monomer unidirectionally diffused into the organic solution, that is, *n*-butanol, the diffusion of the HBAB monomers inside *n*-butanol is of vital significance to the formation of HBAB-TAPA-COF layers. Thus, the diffusion coefficients of HBAB and TAPA monomers in *n*-butanol were calculated based on the analysis of mean-squared displacement (MSD) (Fig. 6f). The diffusion coefficient of the HBAB monomer in *n*-butanol was 1.7×10^{-10} m^2 s^{-1}, three times higher than that of the TAPA monomer (4.4×10^{-11} m^2 s^{-1}), demonstrating the fast diffusion of the HBAB monomer in the organic phase.

On the basis of the microscopic studies and simulations presented above, the formation of the vertically aligned nanorods of the HBAB-TAPA-COF can be illustrated in four steps (Fig. 7). First, since HBAB monomers can diffuse unidirectionally from the aqueous phase to the organic phase, they would be anchored on the surface of the HPAN substrate via the electrostatic attraction between the quaternary ammonium groups and carboxyl groups. Then, the anchored HBAB monomer reacted with the TAPA monomer in the organic phase to form discretely distributed microcrystals, which can serve as the seeding layer for the subsequent growth of the HBAB-TAPA-COF, as confirmed by SEM imaging previously. Notably, given the fact that HBAB monomers can be captured and then be rapidly released by carboxyl groups, HBAB monomers diffused continuously within the HPAN substrate from the bottom to the top surface, so as to continue the growth of the HBAB-TAPA-COF.

With the progress of the growth, HBAB monomers continuously diffused into the organic phase to react with the TAPA monomer near the substrate surface. Such a local consumption of TAPA monomers would produce a concentration gradient, in which the concentration of TAPA monomers near the substrate surface was lower than the region far from the substrate. Furthermore, due to the HBAB monomer possessing a much higher diffusion coefficient than that of the TAPA monomer in *n*-butanol, as confirmed by MD simulations, the HBAB monomer diffused faster than that of the TAPA monomer in the organic phase. Influenced by the above mentioned facts, HBAB monomers are favorable to diffuse into the deeper region far from the substrate surface to react with those TAPA monomers with relatively high concentrations. As a result, the growth of the HBAB-TAPA-COF in the vertical direction would be largely enhanced compared with that in the planar direction, leading to the formation of vertically aligned nanorods. This is well in line with the results from the microscopic observation (Supplementary Fig. 16), as the thickness/length of the nanorods continued to increase while the diameter did not change markedly, prolonging the synthesis duration.

At the end of the growth, defects on the rear surface were completely repaired to afford ultrathin-dense layers due to the extended synthesis duration, as proven by the previous SEM imaging. The extended synthesis duration also allowed the improvement of the crystallinity and porosity of the HBAB-TAPA-COF. In addition, the dense and defect-free layer would trigger the self-limiting effect to terminate the growth of the HBAB-TAPA-COF. Overall, the concentration gradient of TAPA monomers near the substrate surface and the fast diffusion of HBAB monomers in *n*-butanol are the two critical factors. The former originated from the unique molecular structure of HBAB monomers and the mediating effect of the HPAN substrate. The latter stemmed from the unique molecular structure of HBAB monomers. Therefore, the formation of the vertically aligned nanorods of HBAB-TAPA-COF layers was governed by a synergistic effect of the unique molecular structure of HBAB monomers and the mediating effect of the HPAN substrate.

Ion separation performances of HBAB-TAPA-COF membranes

The relationship between the HBAB-TAPA-COF layers and separation performances was revealed by a series of permeation tests[40]. We first examined the integrity of the HBAB-TAPA-COF layers via permeation tests of small organics with a diffusion cell. Different small organics, including anionic organics (Congo red and acid fuchsin), neutral organics (tetracycline and vitamin B12), cationic organics (Rhodamine B and crystal violet) were used as the feed[19,41]. The permeation was driven by the concentration gradient, and the ultraviolet-visible (UV-vis) spectrophotometer was used to record the absorbance of the permeate under different operation times. After the permeation of 3 and 6 h, the appearance of the permeate side showed colorless (Supplementary Fig. 21), and the corresponding UV-vis spectra indicated that small organics did not penetrate through the HBAB-TAPA-COF layers (Supplementary Fig. 22), regardless of their molecular size and charging properties. Thus, the HBAB-TAPA-COF layers were proven to be continuous and defect-free. We then examined the water transport through the HBAB-TAPA-COF layers driven by the osmotic pressure using the same diffusion cell (Supplementary Fig. 23), in which water was used as the feed solution and the 0.5 M sucrose aqueous solution as the draw solution. The HBAB-TAPA-COF layer delivered a superior water flux of 225.4 mol m^{-2} h^{-1}, even though the thickness was large (Supplementary Table 2). The vertically aligned nanorods of the upper part possess enlarged areas to contact with the liquids effectively, and thus water molecules can be adsorbed by the nanopores of the nanorods. The nanorods serve as the harvesters for preferential enriching water molecules, which would further diffuse along the continuous channels within the nanorods to reach the lower part for fast permeation[42]. Meanwhile, water molecules can directly diffuse between the gaps of nanorods to reach the lower part.

We further evaluated the ion sieving capability of the membrane driven by the concentration gradient using the 0.1 M salt solution as the feed (Fig. 8a). A series of chloride salts comprising cations with different hydration diameters, including RbCl, CsCl, KCl, NaCl, LiCl, $CoCl_2$, $CuCl_2$, $SrCl_2$, $MgCl_2$, $LaCl_3$, $CeCl_3$ were examined, and their ionic conductivities on the permeate side linearly increased with the operation time (Supplementary Fig. 24). The permeation rates were then calculated by those linear relations, and were further correlated with the hydration diameter of various cations (Fig. 8b, Supplementary Fig. 25, 26). Cations with higher valences exhibited very low permeation rates, while monovalent cations showed ultrafast permeation rates, and it was as high as 0.36 mol m^{-2} h^{-1} for Rb^+. The permeation rate of various cations followed an order of $Rb^+ > Cs^+ > K^+ > Na^+ > Li^+ > Sr^{2+} > Cu^{2+} > Co^{2+} > Mg^{2+} > La^{3+} > Ce^{3+}$, indicating a sharp cutoff size of 8.2 Å, smaller than the pore size of HBAB-TAPA-COF of 1.2 nm. A simulated mixed-ion system comprising Cs^+,

https://doi.org/10.1038/s41467-024-53625-3

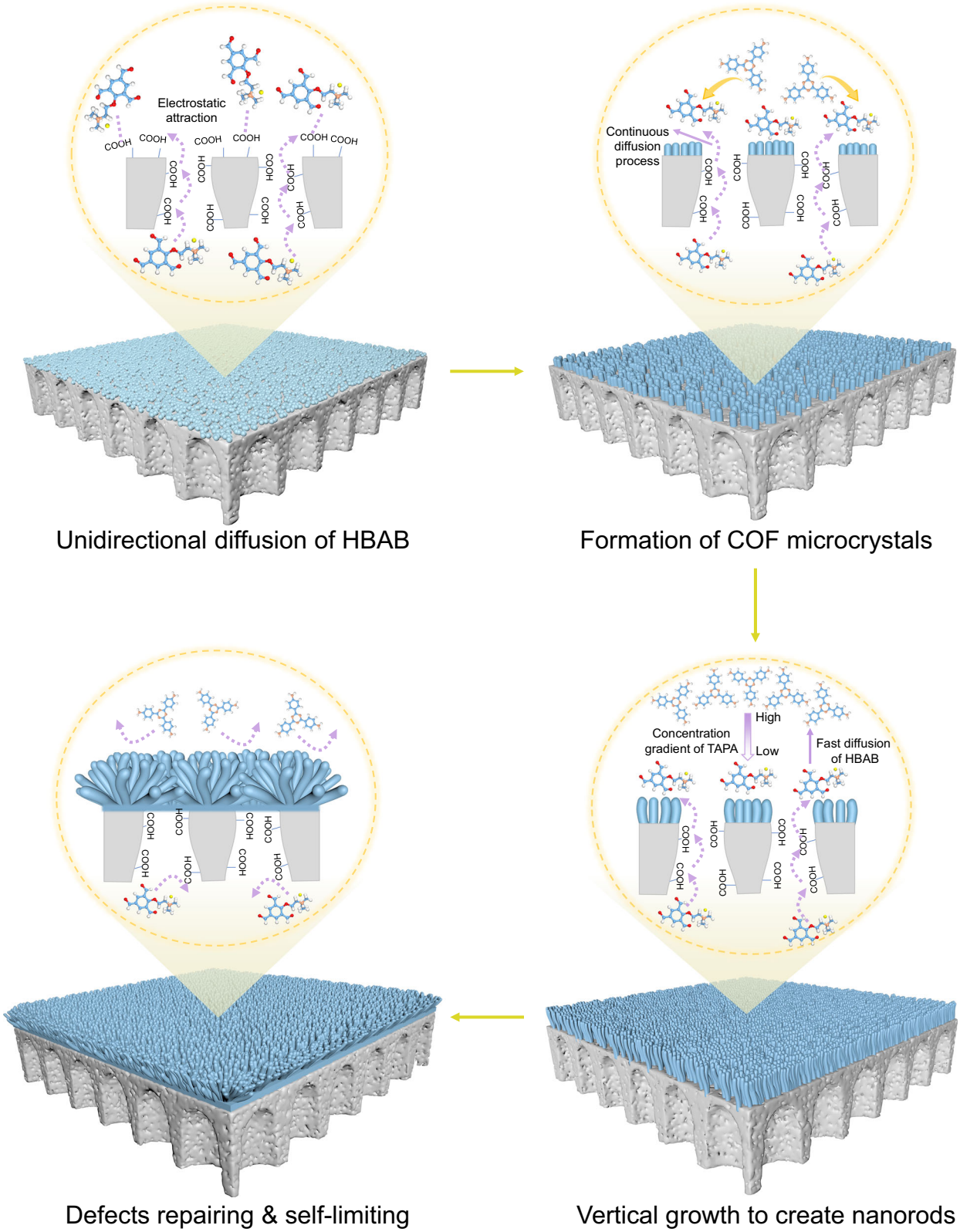

Fig. 7 | Underlying mechanism on the formation of the vertically aligned nanorods of HBAB-TAPA-COF layers. The formation of vertically aligned nanorods involves four key steps: the unidirectional diffusion of HBAB, the formation of COF microcrystals, vertical growth to create nanorods as well as defects repairing and self-limiting.

Sr^{2+}, and La^{3+} was used to evaluate the ion-sieving capability of HBAB-TAPA-COF layers, which is typically involved in the recovery of rare metal ions from aqueous solutions, and is considered a grand challenge[43–47]. For single-ion systems, the HBAB-TAPA-COF layer exhibited high selectivities (S): $S_{Cs+/La3+} = 75.9$, $S_{Cs+/Sr2+} = 14.0$, and $S_{Sr2+/La3+} = 5.4$, and maintained an ultrafast permeation rate for Cs^+ of 0.33 mol m^{-2} h^{-1} (Fig. 8c). For binary-ion systems, the permeation rate of Cs^+ decreased, while the selectivities were slightly dropped to 69.8, 13.3, and 2.1 for Cs^+/La^{3+}, Cs^+/Sr^{2+}, and Sr^{2+}/La^{3+}, respectively (Fig. 8d). Importantly, the selectivity obtained from the binary-ion system did

https://doi.org/10.1038/s41467-024-53625-3

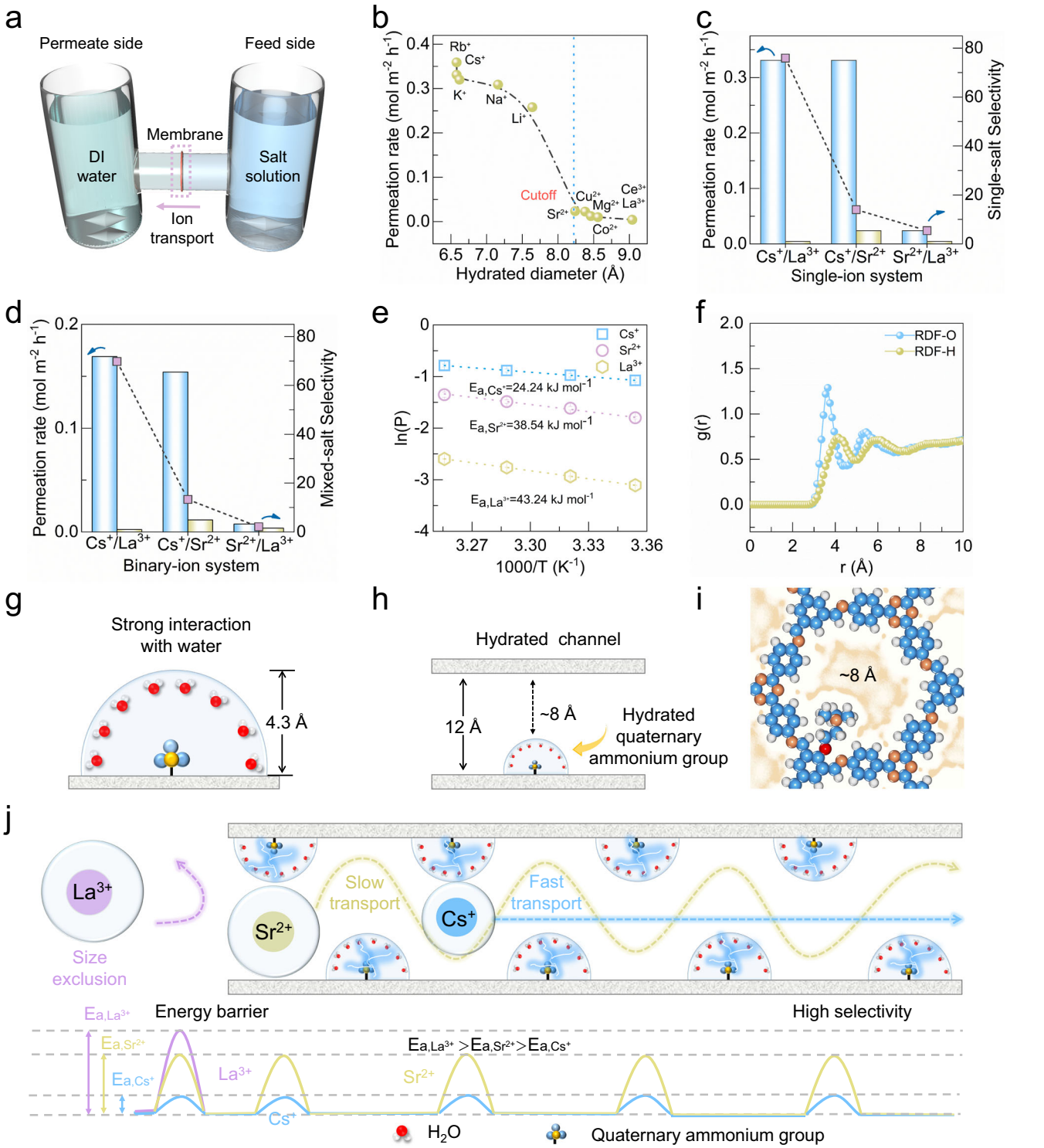

Fig. 8 | Separation performances of HBAB-TAPA-COF layers. a Schematic diagram of the H-shape device used for ion permeation tests. **b** Permeation rate of cations as a function of hydrated ion diameters. The insert shows the cutoff line. Permeation rates and selectivities of **c** single-ion and **d** binary-ion systems. **e** Temperature-dependent permeation rates of cations. The dotted lines show an Arrhenius relationship. **f** RDF of hydrogen and oxygen in water molecules around the quaternary ammonium group located at the pore channel. **g** Schematic illustration of the hydrated quaternary ammonium group and **h** the corresponding channel. **i** Schematic illustration of hydration shells inside the pore channel. **j** Schematic illustration of the possible mechanism for selective transport of cations. Error bars represent the standard deviation of three independent experiments.

not drop significantly compared to that of the single-ion system (Supplementary Table 3), which is better than other membranes, as the selectivity in binary-ion systems is usually much smaller than that in single-ion systems (Supplementary Table 4). Moreover, the HBAB-TAPA-COF layer exhibited excellent reusability in terms of water flux and Cs^+/La^{3+} selectivity after five cycles (Supplementary Table 5).

We further conducted experiments to reveal the relationship between membrane structures and ion-sieving performances. The

mixed-ion system of Cs^+, Sr^{2+}, and La^{3+} was used to evaluate the ion sieving capability of the HBAB-TAPA-COF layers prepared under the synthesis duration of 6, 12, 24, 48, and 72 h, as well as the HPAN substrate (Supplementary Fig. 27). The HPAN substrate showed almost the same permeation rate of ions, along with very poor selectivities: $S_{Cs+}/_{La3+} = 2.0$, $S_{Cs+}/_{Sr2+} = 1.8$, and $S_{Sr2+}/_{La3+} = 1.1$, because of the pore size of the substrate was much larger than the hydrated diameter of ions. When the synthesis duration increased from 6 to 48 h, the permeation rates of ions continued to decrease, but the selectivities were still poor and were close to that of the substrate. These results are well in line with the morphologies observed on the rear surface of the HBAB-TAPA-COF layers, because the defects still existed during these synthesis durations. When the synthesis duration reached 72 h, the permeation rate of ions significantly decreased, and the COF membrane exhibited sharply increased selectivities: $S_{Cs+}/_{La3+} = 75.9$, $S_{Cs+}/_{Sr2+} = 14.0$, and $S_{Sr2+}/_{La3+} = 5.4$ (Supplementary Fig. 28, 29). This is because the dense layer was completely formed, and selective separation can be achieved. Furthermore, we also compared the difference in the ion permeation rate (permeation rate difference) between the substrate and the HBAB-TAPA-COF layers prepared under the different synthesis durations (Supplementary Fig. 30). Surprisingly, the permeation rate of Cs^+ obtained from the HBAB-TAPA-COF layers prepared under 72 h was very close to that of the substrate. On the contrary, the permeation of La^{3+} obtained from the HBAB-TAPA-COF layers prepared under 72 h was ~42 times slower than that of the substrate. This result proved that the ultrathin dense layer of the lower part in the HBAB-TAPA-COF layers enabled fast permeation and high selectivity simultaneously. Above findings revealed a good relationship between membrane structures and ion-sieving performances.

Additionally, we prepared HBAB-TAPA-COF membranes without nanorods to further verify the benefits of our membranes. As shown in Supplementary Fig. 31a, the membrane without nanorods exhibited flat surface composed of nanoparticles, and no significant cracks or pinholes can be observed. From the cross-sectional image (Supplementary Fig. 31b), the membrane was continuous and tightly adhered to the substrate with a thickness of ~23 nm, which is comparable to that of the lower part of the HBAB-TAPA-COF membrane (~29 nm). The membrane without nanorods showed a comparable water flux of 212.2 mol m^{-2} h^{-1} to that of the membrane with nanorods of 225.4 mol m^{-2} h^{-1} (Supplementary Fig. 31c). Considering the almost same thickness of the two membranes, this result proved that the lower part of the HBAB-TAPA-COF membrane mainly accounts for the transport of water across membranes. From Supplementary Fig. 31d, the membrane without nanorods exhibited a selectivity with Cs^+/La^{3+} of 15.8, which is lower than the value of the membrane with nanorods (75.9), but higher than that of the substrate (2.0). Although the membrane without nanorods was continuous to show certain selectivity, the tiny gaps among those nanoparticles on the membrane surface may result in nonselective defects, thus compromising the Cs^+/La^{3+} selectivity to some extent. This result evidenced that the lower part governs the selective separation of ions, and the nanorods of the upper part are necessary to eliminate defects in the lower part.

To gain mechanistic insights into the ion transport through the HBAB-TAPA-COF layers, we performed temperature-dependent ion permeation tests (Fig. 8e). The activation energy (E_a) of Cs^+, Sr^{2+}, La^{3+} was obtained by fitting the data with the Arrhenius equation. The transport of La^{3+} through the HBAB-TAPA-COF layers exhibited a greater E_a (43.24 kJ mol^{-1}) than that of Cs^+ (24.24 kJ mol^{-1}) and Sr^{2+} (38.54 kJ mol^{-1}), implying that La^{3+} needs to overcome a much higher energy barrier to across the HBAB-TAPA-COF layers. When cations entered the intrinsic pore channels of the HBAB-TAPA-COF layers, electrostatic repulsion stemming from the positively charged quaternary ammonium group occurred so that the high-valence cations were subjected to strong repulsion. Therefore, the monovalent cation, Cs^+, could easily enter the pore compared to that of Sr^{2+} and La^{3+}. This result can be confirmed by an ionic conductance test with KCl as the electrolyte (Supplementary Fig. 32). The deviation of ion conductance appeared under low ion concentrations compared to the bulk value, indicating an ion transport behavior governed by surface charges[48].

We further performed MD simulations to reveal the interaction between the quaternary ammonium group and hydrated cations inside the pore channels. The radial distribution function was used to describe the atomic density change with the distance from a certain atom[49]. For water molecules, its oxygen atom showed a closer alignment distance than that of hydrogen atoms (Fig. 8f), indicating that the oxygen atom with electronegativity could strongly bind N^+ in the quaternary ammonium to form a hydration shell with a thickness of 4.3 Å (Fig. 8g). Therefore, the formed hydration shells narrowed the size of the pore channels down to ~8 Å (Fig. 8h, i), which was very closer to that of the aforementioned cutoff size (8.2 Å). Importantly, since the backbone of the HBAB-TAPA-COF is rigid, swelling caused by water molecules inside the pore channel would be strictly restricted[50,51], and the formed nanoconfinement within the one-dimensional channels was favorable for the cation transport (Fig. 8j). The narrowed pore size could effectively exclude La^{3+}, of which the hydrated diameter was 9.0 Å, while Cs^+ (hydrated diameter of 6.6 Å) would pass through. Furthermore, Cs^+ possessed weakly bonded hydration shells, while the hydration shells of Sr^{2+} were tightly bonded due to a stronger electrostatic force of bivalence. When they entered the pore channels, Cs^+ could strip the hydration shell more readily than Sr^{2+} did, allowing itself to fast transport through the pore channels[52]. Notably, these transport behaviors were in accordance with the energy barrier results, as discussed previously. On the basis of the above findings, the vertically aligned nanorods of the HBAB-TAPA-COF layers conferred the ultrafast transport of water and Cs^+, while the nanoconfinement formed inside the pore channels accounted for the excellent selectivity of Cs^+ over La^{3+}.

Discussion

In summary, we reported an engineering concept to synthesize COF membranes with vertically aligned nanorods used for the efficient separation of rare metal ions. A quaternary ammonium-functionalized monomer, HBAB, was first designed and synthesized. Using it as the monomer, the HBAB-TAPA-COF was successfully grown on HPAN substrates to permit vertically aligned nanorods. The HBAB-TAPA-COF nanorods were proven to be porous, crystalline, and mechanically robust. which possessed an asymmetric structure. The upper part displayed vertically aligned nanorods that enlarged contact areas to harvest water and Cs^+, and eliminated the defects. While the lower part exhibited a ~29-nm-thick ultrathin dense layer that ensured both high permeability and selectivity. Moreover, the lower part was sandwiched between the HPAN substrate and vertically aligned nanorods, protecting it from being damaged. The formation of vertically aligned nanorods stemmed from the synergistic effect of monomer structures and porous substrates, as proven by QCM-D measurements and MD simulations. Benefitting from the well-defined structures, the resultant membranes exhibited a high water flux of 225.4 mol m^{-2} h^{-1}, coupled with an ultrafast permeation for Cs^+ of 0.33 mol m^{-2} h^{-1}. Importantly, for the separation of rare metal ions, our membranes showed an exceptional selectivity with Cs^+/La^{3+} of up to 75.9 in a single-ion system, and slightly reduced to 69.8 in a binary-ion system, better than other membranes. This work may inspire a paradigm shift that COF membranes with vertically aligned nanorods are capable of exhibiting extraordinary separation performances, which is of great significance to precise ion separations.

Methods

Materials

Unless otherwise indicated, all chemicals were used without further purification. 2-Hydroxy-1,3,5-benzenetricarbaldehyde (HB, 98%) was

provided by Jilin Chinese Academy of Sciences-Yanshen Technology Co., Ltd. AB (99%) was obtained from Macklin. 2,4,6-Tri(4-aminophenyl)−1,3,5-triazine (TAPA, 98%) was purchased from Heowns. *N*,*N*-Dimethylformamide (DMF, 99%, anhydrous), potassium carbonate (K_2CO_3, 99%), sodium hydroxide (NaOH, 99%), ethyl acetate, *n*-butanol, acetic acid, tetrahydrofuran (THF, 99%), ethanol, various inorganic salts, and small organics were supplied by local suppliers. Polyacrylonitrile (PAN, $Mw = 150\ kg\ mol^{-1}$) was used to prepare porous substrates, following the principle of nonsolvent-induced phase separation. The permeance was ~1500–2000 $L\ m^{-2}\ h^{-1}\ bar^{-1}$. Deionized water was purchased from Wahaha Group Co., Ltd., and used throughout this work.

Synthesis of the HBAB monomer

The quaternary ammonium-functionalized monomer HBAB was synthesized by the Williamson ether reaction. To a Schlenk flask (50 mL), HB (178 mg, 1 mmol), AB (222 mg, 0.9 mmol), and K_2CO_3 (133 mg, 0.9 mmol) were added in succession, and then 20 mL of DMF was charged under nitrogen atmosphere. The mixture was magnetically stirred and was kept at 80 °C for 48 h. After being cooled to room temperature, the insoluble K_2CO_3 was first filtered out, and 20 mL water was added to quench the reaction. Then, ethyl acetate was added into the solution to better dissolve residual HB monomer and was extracted with water three times. The water was removed under reduced pressure at 85 °C using a rotary evaporator, and the solid product was dried under vacuum at 60 °C. Note that it is very difficult to completely remove AB monomer from the product due to their similar polarity, and nevertheless, the residual trace AB monomer does not influence the subsequent synthesis. ^{1}H NMR (400 MHz, DMSO-d6) δ 10.22 (s, 2H), 9.53 (s, 1H), 7.97 (d, $J = 1.0$ Hz, 2H), 3.32 (s, 13H). High-resolution mass spectrometry (HRMS) (m/z): calcd. for $C_{14}H_{18}NO_4Br$, 344.20; found, 264.12 $[M\text{-}Br]^+$.

Preparation of HBAB-TAPA-COF membranes

The HBAB-TAPA-COF membranes were prepared by interfacial synthesis using HPAN membranes as the substrates. HPAN was prepared by soaking PAN substrates in a NaOH aqueous solution (1.5 $mol\ L^{-1}$) at 50 °C for 1 h. After that, the substrates were washed with water thoroughly and stored in water.

Beforehand, two monomer solutions were prepared. HBAB (3 mg, 0.0087 mmol) dissolving in 10 mL water worked as the aqueous phase, and TAPA (3 mg, 0.0085 mmol) dissolving in 10 mL *n*-butanol and acetic acid (50 µL) served as the organic phase. The HPAN substrate was fixed on a homemade synthesis cell, and the upper surface was set to the organic phase side. Subsequently, the two-phase solutions were added simultaneously to both sides of the synthesis cell. After the designated reaction duration, the HBAB-TAPA-COF membranes were obtained. For comparison, the control membrane without nanorods was prepared by changing the solvent from *n*-butanol to a mixture of *o*-dichlorobenzene and dioxane (8 mL: 0.1 mL).

Synthesis of HBAB-TAPA-COF powders

HBAB-TAPA-COF powders were synthesized under solvothermal conditions. Specifically, HBAB (17 mg, 0.05 mmol) and TAPA (18 mg, 0.05 mmol) were added into a glass tube, followed by charging with *n*-butanol (2 mL) and acetic acid aqueous solution (100 µL). The glass tube was frozen in liquid nitrogen, and then subjected to three freeze-pump-thaw cycles. The tube was sealed off under vacuum and was kept at 120 °C for 72 h. After the reaction, the as-obtained dark red powder was collected by filtration and was washed with THF. The final product was obtained after drying under vacuum at 80 °C for 12 h.

Characterizations

The chemical structure of HBAB was examined by the ^{1}H nuclear magnetic resonance spectroscopy (^{1}H NMR, JNM-ECZ400S, JEOL) using deuterated dimethyl sulfoxide (DMSO-d6) as the solvent with the tetramethylsilane internal standard. HRMS data were obtained by Q-Exactive Orbitrap (Thermo Fisher Scientific) in positive mode. FTIR (Nicolet 8700, Thermo Fisher Scientific) was employed to examine the chemical structures of monomers and HBAB-TAPA-COF membranes. The membrane sample was measured in the attenuated total reflectance mode. An XPS (SHIMADZU, AXIS SUPRA) was also employed to examine the chemical structure of HBAB-TAPA-COF membranes. The XRD pattern of samples was recorded on an X-ray diffractometer (Rigaku SmartLab). Field-emission SEM (S-4800, Hitachi) was adopted to observe the morphologies of HBAB-TAPA-COF membranes. The observation was operated at 3 kV, and the samples were sputtered with a thin layer of gold beforehand. N_2 adsorption isotherms of HBAB-TAPA-COF samples were measured on a BELSORP MAX instrument at 77 K. The pore size distribution was calculated using NLDFT model. High-resolution transmission electron microscopy observation was conducted on a JEOL JEM F200 microscope. The surface morphology of the membrane was characterized by AFM. The zeta potentials of membranes were measured under a streaming model using an electrokinetic analyzer (SurPASS, Anton Paar GmbH). The water contact angle was measured on a DSA25S Drop Shape Analyzer (KRÜSS Scientific). GIWAXS measurement was conducted on a Xenocs instrument (Xeuss 3.0). The thermal stability of the membrane was measured on a thermal analyzer (STA449F3, NETZSCH) from room temperature to 800 °C with a ramp rate of 10 °C min^{-1} under a nitrogen atmosphere.

Separation performance tests

All measurements were conducted in an H-shaped diffusion cell consisting of the feed and the permeate compartments, respectively. The membranes were vertically mounted between two compartments and sealed by the spacer rings. The effective membrane area was 0.79 cm^2. For ion permeation tests, 40 mL of inorganic salt solutions (0.1 M) were charged on the feed side, while 40 mL of water was charged on the permeate side, respectively. The ion conductivity of the permeate side was recorded in real-time using an electrical conductivity meter (S230-K, Mettler-Toledo), and the salt concentrations can be derived from their calibration curves. The pH value of salt solutions was controlled at ~6 to prevent any possible hydrolytic precipitation, and the compartments were magnetically stirred to relieve concentration polarization.

The permeation rate J_S ($mol\ m^{-2}\ h^{-1}$) was calculated as follows:

$$J_S = \frac{CV}{A\Delta t} \tag{1}$$

where C ($mol\ L^{-1}$) is the salt concentration of the permeate. V (L) is the volume of the permeate. A (m^2) is the effective area of the membrane. Δt (h) is the permeation duration.

For binary mixtures, the selectivity (S) of monovalent cation/di- or trivalent cations was calculated by the following equation:

$$S = \frac{J_{S^+}}{J_{S^{n+}}} \tag{2}$$

where J_{S^+} and $J_{S^{n+}}$ ($mol\ m^{-2}\ h^{-1}$) are the permeation rates of monovalent, di- or trivalent cations, respectively. The concentration of different cations was determined by inductively coupled plasma mass spectrometry (ICP-MS, Agilent 7800).

Water transport through the membrane was driven by the osmotic pressure difference under a forward osmosis model, in which water (40 mL) and sucrose aqueous solution (40 mL, 0.5 $mol\ L^{-1}$) were used as the feed and the draw solutions, respectively. Specifically, both compartments were equipped with a capillary glass tube to record the volume change. The water flux J_W ($mol\ m^{-2}\ h^{-1}$) was calculated from the volume change ΔV (mL), duration Δt (h), and the effective area of the

membrane A (m^2), based on the following equation:

$$J_w = \frac{\Delta V_\rho}{MA\Delta t} \quad (3)$$

where ρ ($g\ mL^{-1}$) is the water density, and M is the molar mass of water.

Reusability tests were performed by successively measuring the water flux and the Cs^+/La^{3+} selectivity for five cycles, respectively.

Permeation tests using various small organics were conducted in the same H-shaped diffusion cell as described above. Positively charged (rhodamine B, crystal violet), neutral (tetracycline, vitamin B12), and negatively charged (Congo red, acid fuchsin) small organics (40 mL, 25 mg L^{-1}) were filled in the feed side, and 40 mL of water was filled in the permeate side, respectively. Their concentrations after designated durations were determined by a UV-vis spectrophotometer (Nanodrop 2000c, Thermo Fisher Scientific).

Ion current was measured on a Keithley 6487 picoammeter (Keithley Instruments) with a pair of Ag/AgCl electrodes used to apply transmembrane potentials. The scanning voltage ranging from −1 to +1 V was used. The pH value of different electrolyte solutions was maintained at ~6.

QCM-D analysis

Quartz crystal microbalance with dissipation (QCM-D, QSense Explorer, Biolin Scientific) was used to monitor the adsorption and release of HBAB monomer. Prior to testing, samples were prepared by coating PAN onto sensors having gold-coated AT-cut quartz crystals. To prepare the PAN-coated sensor, PAN powders were dissolved in *N*,*N*-dimethylformamide to form a homogenous solution with a concentration of 12 wt%. A 100 µL of PAN solution was dropped onto the sensor, followed by spin-coating (3000 rpm, 15 s). The sensor was then soaked in water to trigger phase inversion, and the PAN sample can be obtained. For HPAN sample, as-prepared PAN-coated senor was immersed in a NaOH aqueous solution (1.5 mol L^{-1}) at 50 °C for 30 min, followed by water washing.

To implement the tests, sensors were mounted into the flow module of QCM-D, followed by flowing water for at least 1 h to establish the baseline. All measurements were conducted at a flow rate of 80 µL min^{-1} with a temperature of 25 °C. A HBAB aqueous solution (100 mg L^{-1}) was first injected into the module to conduct the adsorption test. After reaching the adsorption equilibrium, water was then injected so as to conduct the release test. Frequency changes throughout the measurement were recorded in real-time, and were derived into the mass variation of HBAB by the Sauerbrey equation:

$$\Delta f = -\frac{2f_0^2}{A\sqrt{\rho_q \mu_q}} \times \Delta m \quad (4)$$

where Δf (Hz) is the frequency, f_0 (Hz) is the resonant frequency of the sensor, A (m^2) is the piezoelectrically active crystal area, ρ_q ($kg\ m^{-3}$) is the density of quartz, μ_q (Pa) is the shear modulus of the quartz, and Δm (kg) changes in mass adsorbed on the sensor.

Note that, although the membrane structure of samples may not be the same as that in the preparation of HBAB-TAPA-COF membranes, it still offers a means to quantify the adsorption and release of HBAB monomer.

MD simulation

All MD simulations were performed using the Large-scale Atomic/Molecular Massively Parallel Simulator (LAMMPS) package[53]. The unit cell of HBAB-TAPA-COF was optimized using the generalized gradient approximation exchange-correlation function defined by Perdew, Burke, and Ernzerhof. The Dreiding force field (DREIDING: a generic force field for molecular simulations) was used for HBAB-TAPA-COF to simulate the interaction among atoms. Restrained electrostatic potential (RESP) charges were used to describe the atomic partial charges of HBAB-TAPA-COF. The RESP charges were calculated under the implicit solvent environment of water using B3LYP exchange-correlation functional in conjunction with 6–311 G (d,p) basis set and analyzed by the Multiwfn software[54]. Water molecules were modeled using the SPC/E potential[55], and the bonds and angles of water were constrained by the SHAKE algorithm. For all dynamics runs, the temperature was controlled using the Nosé–Hoover thermostat, and the pressure was controlled with the Berendsen barostat. The LJ and Coulombic parameters of ions and other molecules were described by the optimized potentials for liquid simulations-all atoms[56]. The Lorentz-Berthelot mixing rule was used to calculate pair-wise LJ parameters. Cutoff distances for LJ and Coulomb interactions were set to 1.0 and 1.2 nm, respectively. Particle-particle-mesh solver with a root-mean-square error of 10^{-4} was used to calculate long-range electrostatic interactions. Initially, energy minimization was utilized to eliminate atom overlaps. Following that, each simulation process began with a 5 ns pre-equilibration process. Each simulation system ran for at least 10 ns with a time step of 1 fs. The results were visualized using the VMD[57], and the simulation trajectories were saved every 1 ps for further analysis.

Data availability

The authors declare all data supporting the findings of this study are available within the article and supplementary Information file, and additional data are available from the corresponding author upon request. Source data are provided with this paper.

References

1. Lv, J. et al. Direct Solar-to-electrochemical energy storage in a functionalized covalent organic framework. *Angew. Chem. Int. Ed.* **57**, 12716–12720 (2018).
2. Zhao, X., Pachfule, P. & Thomas, A. Covalent organic frameworks (COFs) for electrochemical applications. *Chem. Soc. Rev.* **50**, 6871–6913 (2021).
3. Liu, R. et al. Covalent organic frameworks: an ideal platform for designing ordered materials and advanced applications. *Chem. Soc. Rev.* **50**, 120–242 (2021).
4. Wang, Z., Zhang, S., Chen, Y., Zhang, Z. & Ma, S. Covalent organic frameworks for separation applications. *Chem. Soc. Rev.* **49**, 708–735 (2020).
5. Qu, Z. et al. Pore engineering in covalent organic framework membrane for gas separation. *Adv. Membr.* **2**, 100037 (2022).
6. Li, Z., He, T., Gong, Y. & Jiang, D. Covalent organic frameworks: pore design and interface engineering. *Acc. Chem. Res.* **53**, 1672–1685 (2020).
7. Evans, A. M. et al. Two-dimensional polymers and polymerizations. *Chem. Rev.* **122**, 442–564 (2021).
8. Huang, N., Zhai, L., Xu, H. & Jiang, D. Stable covalent organic frameworks for exceptional mercury removal from aqueous solutions. *J. Am. Chem. Soc.* **139**, 2428–2434 (2017).
9. Yin, C. et al. Azo-branched covalent organic framework thin films as active separators for superior sodium-sulfur batteries. *ACS Nano* **16**, 14178–14187 (2022).
10. Diercks, C. S. & Yaghi, O. M. The atom, the molecule, and the covalent organic framework. *Science* **355**, aal1585 (2017).
11. Wang, H. et al. Organic molecular sieve membranes for chemical separations. *Chem. Soc. Rev.* **50**, 5468–5516 (2021).
12. Wang, R. et al. Unidirectional diffusion synthesis of covalent organic frameworks (COFs) on polymeric substrates for dye separation. *J. Membr. Sci.* **586**, 274–280 (2019).
13. Tan, Z., Chen, S., Peng, X., Zhang, L. & Gao, C. Polyamide membranes with nanoscale Turing structures for water purification. *Science* **360**, 518–521 (2018).

14. Geng, K. et al. Covalent organic frameworks: design, synthesis, and functions. *Chem. Rev.* **120**, 8814–8933 (2020).
15. Ren, L., Chen, J., Han, J., Liang, J. & Wu, H. Biomimetic construction of smart nanochannels in covalent organic framework membranes for efficient ion separation. *Chem. Eng. J.* **482**, 148907 (2024).
16. Fenton, J. L., Burke, D. W., Qian, D. & Dichtel, W. R. Polycrystalline covalent organic framework films act as adsorbents, not membranes. *J. Am. Chem. Soc.* **143**, 1466–1473 (2021).
17. Sasmal, H. S. et al. Superprotonic conductivity in flexible porous covalent organic framework membranes. *Angew. Chem. Int. Ed.* **57**, 10894–10898 (2018).
18. Chen, T. et al. Highly crystalline ionic covalent organic framework membrane for nanofiltration and charge-controlled organic pollutants removal. *Sep. Purif. Technol.* **256**, 117787 (2021).
19. Zhang, W., Zhang, L., Zhao, H., Li, B. & Ma, H. A two-dimensional cationic covalent organic framework membrane for selective molecular sieving. *J. Mater. Chem. A.* **6**, 13331–13339 (2018).
20. Zhang, Z. et al. Heterostructured two-dimensional covalent organic framework membranes for enhanced ion separation. *Chem. Commun.* **58**, 7136–7139 (2022).
21. Sheng, F. et al. Efficient ion sieving in covalent organic framework membranes with sub-2-nanometer channels. *Adv. Mater.* **33**, 2104404 (2021).
22. Liu, L. et al. Surface-mediated construction of an ultrathin free-standing covalent organic framework membrane for efficient proton conduction. *Angew. Chem. Int. Ed.* **60**, 14875–14880 (2021).
23. Yang, J. et al. Advancing osmotic power generation by covalent organic framework monolayer. *Nat. Nanotechnol.* **17**, 622–628 (2022).
24. Sahabudeen, H. et al. Highly crystalline and semiconducting imine-based two-dimensional polymers enabled by interfacial synthesis. *Angew. Chem. Int. Ed.* **59**, 6028–6036 (2020).
25. You, X. et al. Charged nanochannels in covalent organic framework membranes enabling efficient ion exclusion. *Acs. Nano* **16**, 11781–11791 (2022).
26. Wang, M. et al. Ultrafast seawater desalination with covalent organic framework membranes. *Nat. Sustain.* **5**, 518–526 (2022).
27. Wang, R. et al. Ultrathin covalent organic framework membranes prepared by rapid electrophoretic deposition. *Adv. Mater.* **34**, 2204894 (2022).
28. Wang, X. et al. Electrosynthesis of ionic covalent organic frameworks for charge-selective separation of molecules. *Small* **18**, 2107108 (2022).
29. Yanbing, Y. et al. Large-area graphene-nanomesh/carbon-nanotube hybrid membranes for ionic and molecular nanofiltration. *Science* **364**, 1057–1062 (2019).
30. Yang, Y. et al. Elastic films of single-crystal two-dimensional covalent organic frameworks. *Nature* **630**, 878–883 (2024).
31. Matsumoto, M. et al. Lewis-acid-catalyzed interfacial polymerization of covalent organic framework films. *Chem* **4**, 308–317 (2018).
32. Knebel, A. & Caro, J. Metal-organic frameworks and covalent organic frameworks as disruptive membrane materials for energy-efficient gas separation. *Nat. Nanotechnol.* **17**, 911–923 (2022).
33. Dong, Z., Zhang, L., Gong, J. & Zhao, Q. Covalent organic framework nanorods bearing single Cu sites for efficient photocatalysis. *Chem. Eng. J.* **403**, 126383 (2021).
34. Gong, H. et al. Tunable 1D and 2D polyacrylonitrile nanosheet superstructures. *Acs. Nano* **17**, 18392–18401 (2023).
35. Yin, C. et al. Perpendicular alignment of covalent organic framework (COF) pore channels by solvent vapor annealing. *J. Am. Chem. Soc.* **145**, 11431–11439 (2023).
36. Zhu, C. et al. Manipulating charge density in nanofluidic membranes for optimal osmotic energy production density. *Adv. Funct. Mater.* **32**, 2109210 (2021).
37. Lu, Q. et al. Postsynthetic functionalization of three-dimensional covalent organic frameworks for selective extraction of lanthanide ions. *Angew. Chem. Int. Ed.* **57**, 6042–6048 (2018).
38. Yang, Z. et al. Tannic acid/Fe^{3+} nanoscaffold for interfacial polymerization: toward enhanced nanofiltration performance. *Environ. Sci. Technol.* **52**, 9341–9349 (2018).
39. Zhou, X. et al. Intrapore energy barriers govern ion transport and selectivity of desalination membranes. *Sci. Adv.* **6**, eabd9045 (2020).
40. Xu, T. et al. Highly ion-permselective porous organic cage membranes with hierarchical channels. *J. Am. Chem. Soc.* **144**, 10220–10229 (2022).
41. Kandambeth, S. et al. Selective molecular sieving in self-standing porous covalent-organic-framework membranes. *Adv. Mater.* **29**, 1603945 (2016).
42. Xu, T. et al. Highly cation permselective metal-organic framework membranes with leaf-like morphology. *ChemSusChem* **12**, 2593–2597 (2019).
43. Yuan, T., Xiong, S. & Shen, X. Coordination of actinide single ions to deformed graphdiyne: strategy on essential separation processes in nuclear fuel cycle. *Angew. Chem. Int. Ed.* **59**, 17719–17725 (2020).
44. Feng, M. L. et al. Efficient removal of $[UO_2]^{2+}$, Cs^+, and Sr^{2+} ions by radiation-resistant gallium thioantimonates. *J. Am. Chem. Soc.* **140**, 11133–11140 (2018).
45. Zhao, Y. M. et al. pH-Controlled switch over coadsorption and separation for mixed Cs^+ and Sr^{2+} by an acid-resistant potassium thioantimonate. *Adv. Funct. Mater.* **32**, 2112717 (2022).
46. Wang, Z. et al. Ion sieving in graphene oxide membrane enables efficient actinides/lanthanides separation. *Nat. Commun.* **14**, 261 (2023).
47. Sholl, D. & Lively, R. Seven chemical separations to change the world. *Nature* **532**, 435–437 (2016).
48. Xin, W. et al. Biomimetic KcsA channels with ultra-selective K^+ transport for monovalent ion sieving. *Nat. Commun.* **13**, 1701 (2022).
49. Xu, F., Wei, M., Zhang, X. & Wang, Y. Ion rejection in covalent organic frameworks: revealing the overlooked effect of in-pore transport. *Acs. Appl. Mater. Interfaces* **11**, 45246–45255 (2019).
50. Cao, L. et al. Weakly humidity-dependent proton-conducting COF membranes. *Adv. Mater.* **32**, 2005565 (2020).
51. Kang, Y. et al. Functionalized 2D membranes for separations at the 1-nm scale. *Chem. Soc. Rev.* **53**, 7939–7959 (2024).
52. Xu, T. et al. Perfect confinement of crown ethers in MOF membrane for complete dehydration and fast transport of monovalent ions. *Sci. Adv.* **10**, eadn0944 (2024).
53. Plimpton, S. Fast parallel algorithms for short-range molecular dynamics. *J. Comput. Phys.* **117**, 1–19 (1995).
54. Lu, T. & Chen, F. Multiwfn: a multifunctional wavefunction analyzer. *J. Comput. Chem.* **33**, 580–592 (2011).
55. Berendsen, H. J. C. & Straatsma, T. P. The missing term in effective pair potentials. *J. Phys. Chem.* **91**, 6269–6271 (1987).
56. Jorgensen, W. L. & Maxwell, D. S. Development and testing of the OPLS all-atom force field on conformational energetics and properties of organic liquids. *J. Am. Chem. Soc.* **118**, 11225–11236 (1996).
57. Dalke, A. & Schulten, K. VMD: visual molecular dynamics. *J. Mol. Graph.* **14**, 33–38 (1996).

Acknowledgements

Financial support from the National Natural Science Foundation of China, Grant No. 21921006 (Y.W.), 22308147 (Z.Z.), 22278206 (M.W.).

Author contributions

Y.W. and Z.Z. conceived the project and methodology. Q.L. carried out the experiments and structural characterizations. M.L. and M.W. performed the MD simulations. J.L. helped to perform structural characterizations. C.Y. provided suggestions for results. All authors contributed to the discussions. Q.L., Z.Z., and Y.W. co-wrote the manuscript.

Competing interests
The authors declare no competing interests.

Additional information
Supplementary information The online version contains supplementary material available at https://doi.org/10.1038/s41467-024-53625-3.

Correspondence and requests for materials should be addressed to Zhe Zhang or Yong Wang.

Peer review information *Nature Communications* thanks Heping Ma and the other, anonymous, reviewer(s) for their contribution to the peer review of this work. A peer review file is available.